

Scalable Semitransparent Prototype Organic Photovoltaic Module with Minimal Resistance Loss

Xinjing Huang¹, Dejiu Fan², and Stephen R. Forrest^{1,2,3}

1. Applied Physics Program,

2. Department of Electrical Engineering and Computer Science,

3. Department of Physics, Department of Material Science and Engineering

University of Michigan, Ann Arbor, MI, 48109 United States

Abstract

Semi-transparent organic photovoltaic (ST-OPV) cells are regarded as an attractive solution to building-integrated solar energy harvesting. Both the power conversion efficiency (*PCE*) and average photopic transmission (*APT*) of ST-OPVs have shown substantial increases in recent years. However, less attention has been paid to the area scaling of ST-OPV cells. In this work, we investigate the scalability of ST-OPV cells from 4 mm² to 1 cm², as well as 9 cm² active area prototype module. By integrating both top and bottom metal grids onto the transparent electrodes, the series resistance loss of 1 cm² ST-OPV cell is significantly reduced, and is comparable to that of the grid-free 4 mm² cell. Nine 1 cm² cells are then connected in a series-parallel circuit to realize a prototype ST-OPV module. A 100% fabrication yield with only 5% *PCE* deviation among discrete cells is achieved. The semitransparent module shows $PCE = 7.2 \pm 0.1\%$ under simulated AM 1.5G illumination at 1 sun intensity, which exhibits no connection resistance loss compared to that of the individual cells. The ST-OPV module exhibits an $APT = 38.1 \pm 1.1\%$, which enables a light utilization efficiency, $LUE = 2.74 \pm$

0.09%. The method demonstrates a promising way for ST-OPV modules to scale without compromising performance.

Introduction

Building integrated photovoltaics (BIPV) that employ transparent solar cells on window panes provide a space-efficient and attractive solution to solar energy harvesting.^{1–5} Unlike conventional inorganic semiconductors, organic semiconductors have relatively narrow excitonic absorption spectra that allow for organic photovoltaics (OPV) featuring transparency across visible spectrum, while selectively absorbing in the near-infrared (NIR).^{6–8} In this regard, OPVs are an attractive BIPV technology that can simultaneously achieve a high power conversion efficiency (*PCE*) along with a high average photopic transmission (*APT*). Over the past few years, OPVs have been demonstrated with impressive *PCE* and exceptional intrinsic stability.^{9–13} Furthermore, with the development of NIR-absorbing materials and optical structures, semitransparent OPVs (ST-OPVs) have realized remarkable improvements in light utilization efficiency ($LUE = PCE \times APT$) up to 5.0%.^{14–22} Starting from this promising performance, an estimated cost of 0.47 - 1.6 \$/W_p has been reported,²³ which motivates practical and widespread deployment of ST-OPVs in BIPV applications.

It remains questionable, however, whether these highly efficient laboratory-scale, small-area ST-OPVs can maintain their performance when translated to larger modules. To date, research on OPV modules has primarily focused on multi-junction strategies and improved material design in opaque devices,^{24,25} while less attention has been paid to the scalability of ST-OPVs.^{26–34} Compared to opaque OPVs with one thick, highly conductive metal electrode, ST-OPVs require both electrodes to be transparent, which doubles the overall series resistance loss, and significantly limits their scalability. Moreover, the narrow energy gaps of NIR-

absorbing materials required in ST-OPVs result in a low open-circuit voltage (V_{OC}), which worsens series resistance losses by reducing the fill factor (FF) and, ultimately, the PCE .^{24,35}

Here, we demonstrate a scalable ST-OPV prototype module with a negligible compromise of efficiency from series resistance losses. The ST-OPVs employ bulk heterojunction (BHJ) based on a low energy gap polymer donor, poly[4,8-bis(5-(2-ethylhexyl)thiophen-2-yl)benzo[1,2-b:4,5-b']dithiophene-co-3-fluorothieno[3,4-b]thiophene-2-carboxylate] (PCE-10), combined with a NIR absorbing acceptor, (4,4,10,10-tetrakis(4-hexylphenyl)-5,11-(2-ethylhexyloxy)-4,10-dihydro-dithienyl[1,2-b:4,5b']benzodi-thiophene-2,8-diyl)bis-(2-(3-oxo-2,3-dihydroinden-5,6-dichloro-1-ylidene)-malononitrile) (BT-CIC).⁸ As the active area of the cells scale from 4 mm² to 1 cm², the sheet resistance of the indium tin oxide (ITO) cathode and the thin, semitransparent Ag anode dominates the specific series resistance (R_sA), which reduces the FF and PCE . By employing finely patterned metal grids on the two transparent electrodes,^{36–40} the series resistance loss of 1 cm² device is significantly reduced, leading to an improved PCE close to that of a 4 mm² device. Based on these findings, nine 1 cm² ST-OPV devices are integrated into a prototype module and connected in a series-parallel circuit configuration²⁴ with a geometric fill factor (GFF) of 65%. A 100% fabrication yield with cell-to-cell PCE variation of < 5% is achieved. The module performance shows no loss from connection resistance compared to the discrete cells. Combined with an optimized visible light outcoupling (OC) structure, the ST-OPV module exhibits $LUE = 2.74 \pm 0.09\%$ with $APT = 38.1 \pm 1.1\%$ and $PCE = 7.2 \pm 0.1\%$ under simulated AM 1.5G illumination at 1 sun intensity. With the combination of NIR absorbing BHJ, OC structure and minimized resistance loss in

module construction, this is a significant improvement over previous reported ST-OPV module performance.^{25–34}

Results and Discussion

Figure 1 shows a schematic illustration of the 1 cm² ST-OPV structure, which employs a 80 nm PCE-10:BT-CIC (1:1.5 w/w) BHJ, with 30 nm thick ZnO and 20 nm thick MoO_x as electron and hole transporting layers, respectively. To investigate the resistance loss from the bottom ITO cathode with area scaling, we fabricated opaque OPV devices with 100 nm thick top Ag anode. The current density-voltage (J - V) characteristics are shown in Fig. 2(a), with detailed performance parameters listed in Table I. The 4 mm² opaque device (red line with squares) has $R_{SA} = 1.5 \pm 0.1 \text{ } \Omega \cdot \text{cm}^2$, however, the R_{SA} increases to $15.4 \pm 0.5 \text{ } \Omega \cdot \text{cm}^2$ as the active area increases to 1 cm² (blue line with circles) due to the 15 Ω/sq large sheet resistance of ITO, which results in a significant decrease in FF from 0.69 ± 0.01 to 0.39 ± 0.03 . To reduce the R_{SA} from ITO, we integrate a 500 nm thick Au surrounding and 50 nm thick Au grids onto the ITO cathode, as shown for the bottom electrode in Fig. 1. The nearly invisible grids are patterned into 20 μm wide stripes with 400 μm separation via photolithography (see Experimental for details). The grids reduce R_{SA} of the 1 cm² opaque device (yellow line with triangles) to $3.1 \pm 0.4 \text{ } \Omega \cdot \text{cm}^2$, leading to $FF = 0.65 \pm 0.01$. Although the short-circuit current density (J_{SC}) is decreased from $23.1 \pm 0.7 \text{ mA/cm}^2$ to $22.0 \pm 0.4 \text{ mA/cm}^2$ because the Au grids partially block the light incident on the photoactive region, a significant increase in PCE from $5.9 \pm 0.3\%$ to $10.0 \pm 0.2\%$ is realized.

The 1 cm² ST-OPV devices with a 16 nm thick, semitransparent Ag anode was fabricated, with J - V characteristics shown in Fig. 2(b) and parameters listed in Table I. Compared to 4

mm² devices (red line with squares) with $R_{SA} = 1.8 \pm 0.1 \text{ } \Omega \cdot \text{cm}^2$, the 1 cm² ST-OPV with integrated bottom electrode (blue line with circles) shows $R_{SA} = 9.5 \pm 0.3 \text{ } \Omega \cdot \text{cm}^2$, indicating that the resistance is mainly due to the ultrathin Ag anode which has sheet resistance of 6 Ω/sq . As illustrated in Fig. 1, we deposited a layer of 100 nm thick Ag top grids with 20 μm grid width and 600 μm separation patterned using a 25 μm thick Kapton shadow mask. Compared to conventional metal shadow mask, the thin Kapton mask allows for ultrafine resolution patterning. The fabrication flow of the Kapton shadow mask is illustrated in Experimental section. The reflection from the 100 nm Ag grids provides a slight increase in the J_{SC} of 1 cm² ST-OPV from $16.2 \pm 0.3 \text{ mA/cm}^2$ to $16.5 \pm 0.1 \text{ mA/cm}^2$. The R_{SA} of the 1 cm² ST-OPV (yellow line with triangles) is reduced to $4.3 \pm 0.2 \text{ } \Omega \cdot \text{cm}^2$, which leads to an increase in FF from 0.57 ± 0.01 to 0.65 ± 0.01 , and the PCE from $6.3 \pm 0.2\%$ to $7.3 \pm 0.1\%$.

The 1 cm² ST-OPV shown in Fig. 1 combines the bottom and top grid electrodes with the 4-layer OC structure comprising ZnS (30 nm)/MgF₂ (100 nm)/4,4'-Bis(N-carbazolyl)-1,1'-biphenyl (CBP) (90 nm)/MgF₂ (10 nm) at the top surface to improve visible transmission. The integration of grids on both electrodes occupies 7% of the device active area and blocks the view directly behind the grids. Figures 2(c) and (d) show the J - V characteristics and external quantum efficiency (EQE) spectra of the 1 cm² ST-OPV with and without the OC structure, and the detailed parameters are provided in Table I. The transmission and reflection spectra of the ST-OPV stack with and without the OC layers are plotted in Fig. 2(e). The OC structure significantly increases the transmission of ST-OPV in the visible, which results in an improved APT from $20.0 \pm 1.0\%$ to $38.1 \pm 1.1\%$, while $PCE = 7.3 \pm 0.1\%$ is maintained.

We then fabricated a small prototype module comprising nine, 1 cm² ST-OPVs cells with both grids and OC structures. As shown in Fig. 3, three discrete cells are series connected with a 0.3 cm interconnection distance to form a column, while three columns are separated by 0.25 cm, and are connected in parallel with the contact electrodes to construct the module. This design has a $GFF = 65\%$, which is limited by the width of bottom electrode Au surrounding bar, and the use of mechanical scribing to pattern the heterojunction layers. By increasing the Au side bar thickness, the width can be narrowed without affecting performance. Mechanical scribing can also be replaced with higher resolution laser scribing to further improve the GFF .⁴¹

The fabrication yield of discrete cells is 100%. Under 1 sun illumination, the nine individual cells exhibit short-circuit currents of $I_{SC} = 16.8 \pm 0.1$ mA, $V_{OC} = 0.67 \pm 0.01$ V, $FF = 0.63 \pm 0.01$. All the parameters have cell-to-cell variations of $< 5\%$. The PCE of the discrete cells ranges within $7.2 \pm 0.2\%$, as shown in Fig. 4(a). Figure 4(b) shows the current-voltage (I - V) characteristics of a discrete cell and the module, with detailed parameters shown in Table I. We obtain a module output power of 65 ± 3 mW under simulated AM 1.5G at 1 sun intensity, with $I_{SC} = 51.1 \pm 1.0$ mA, $V_{OC} = 2.00 \pm 0.01$ V and $FF = 0.63 \pm 0.01$, corresponding to $PCE = 7.2 \pm 0.1\%$ in reference to the active area of the prototype module. The module V_{OC} is 0.5% less than the sum of the V_{OC} of three individual cells, while I_{SC} is within 1.5% deviation from the sum of three individual cells. Also, FF is the same as for the discrete cells, indicating that the resistance losses from electrodes and interconnections are minimal due to the metal grids and circuit layout. Combined with the optimized transmission $APT = 38.1 \pm 1.1\%$, we obtain a module $LUE = 2.74 \pm 0.09\%$. A photograph of the ST-OPV module is shown in the inset of Fig. 4(b).

Note that here we only report on a prototype module as a means to study the effect of scaling on resistance. Our results indicate that if high resolution electrode patterning is used, the GFF can approach unity, in which case the reported $PCE = 7.2 \pm 0.1\%$ would also be achieved in a practical module. Furthermore, note that the ST-OPV module overcomes the efficiency loss from connection resistance as more cells are connected even in opaque OPV modules.^{41,42} Our result suggests that with the foregoing fabrication process, ST-OPV modules with increased number of columns and rows can have an increased V_{OC} and I_{SC} without degradation of either FF or PCE .

Conclusion

We investigated the effect of series resistance loss on the scalability of ST-OPV devices. Compared to 4 mm² devices, the dominant contribution from ITO cathode and ultrathin Ag anode sheet resistance results in a significantly increased resistive loss in 1 cm² ST-OPV cells. By integrating Au grids onto the cathode and Ag grids onto the anode, the R_sA is reduced such that the PCE loss is negligible. Furthermore, with the application of a series-parallel circuit layout, we demonstrated a 9 cm² active area, prototype ST-OPV module with 100% discrete cell yield and a PCE variation within 5% across the module. The ST-OPV module exhibits $PCE = 7.2 \pm 0.1\%$, which has no loss compared to discrete cells performance, $APT = 38.1 \pm 1.1\%$, and $LUE = 2.74 \pm 0.09\%$. This demonstration provides a promising path for ST-OPV modules to achieve unlimited scalability with uncompromised module performance.

Experimental

Materials

All materials were purchased from vendors: PCE-10 and BT-CIC from 1-Material Inc. (Quebec, Canada), MoO₃ was from Acros Organics (NJ, USA), Ag from Alfa Aesar (MA, USA), MgF₂ and ZnS from Kurt J. Lesker Corp. (PA, USA) and CBP from Luminescence Technology Corp. (Taiwan).

Au grids/ITO cathode fabrication

Glass substrates were cleaned with detergent and solvents before deposition. A 150 nm thick ITO layer was sputter-deposited at 1.72 Å/s in a high vacuum chamber (base pressure $\sim 10^{-7}$ Torr) and thermally annealed at 400 °C for 5 min in forming gas (5% H₂ + 95% N₂). The ITO was photolithographically patterned and wet etched using HCl:H₂O (3:1) to define the square shaped cathode. The Au surrounding bars (0.5 mm wide, 200 nm thick on a pre-deposited 10 nm thick Ti adhesion layer) are photolithographically patterned along three edges of the ITO cathode, and Au grids (20 µm wide, 400 µm separation, 45 nm thick with a 5 nm thick Ti adhesion layer) are patterned across the entire cathode. All Au and Ti layers were deposited via electron-beam evaporation at 5 Å/s. For the module, nine cathode squares were patterned into 3 columns and 3 rows.

Kapton shadow mask preparation

As described in Fig. 5, a 25 µm thick E-type Kapton foil is coated with 10 nm thick Ti/500 nm Al using electron-beam evaporation. A 100 µm thick PDMS (Sylgard 184, base-to-curing agent weight ratio = 10: 1) membrane is spun at 800 rpm on a 10 cm diameter Si handle and

cured at 100 °C for 3 h. The Kapton foil with Al layer facing up is then attached to the PDMS membrane to eliminate curling. The top grid pattern (20 μm wide, 600 μm separation) is photolithographically defined on the foil. The foil is etched using Cl_2 plasma ($\text{H}_2:\text{Cl}_2:\text{Ar} = 12:9:5$ sccm, 10 mTorr chamber pressure, 500 W inductively coupled plasma (ICP) power, 100 W forward power for 1 min) to remove the Ti and Al layers and expose the Kapton. The 25 μm Kapton foil is then etched through using O_2 plasma ($\text{O}_2 = 20$ sccm, 6 mTorr chamber pressure, 500 W ICP power, 100 W forward power for 40 min). Finally, the Kapton foil is detached from the PDMS membrane and soaked in buffered HF for 6 min to remove the remaining Al and Ti.

Device fabrication and characterization

Glass substrates with a patterned cathode (ITO or Au/ITO) were cleaned using detergent and solvents followed by UV ozone exposure for 15 min before growth. The ZnO precursor solution was spin-coated onto the substrate at 3000 rpm and baked at 160 °C in air for 30 min. The PCE-10:BT-CIC solution was prepared in chlorobenzene with 10% chloroform at a concentration of 16 mg/mL and stirred overnight at 65 °C, 350 rpm. After filtering through a 0.45 μm polytetrafluoroethylene filter, the solution was spin-coated at 2000 rpm on top of ZnO layer in ultrapure N_2 ($\text{O}_2 < 0.1$ ppm, $\text{H}_2\text{O} < 0.1$ ppm). Then the samples were transferred into a high vacuum chamber (base pressure $\sim 10^{-7}$ Torr) for thermal evaporation of 20 nm thick MoO_x at 0.2 $\text{\AA}/\text{s}$. For 1 cm^2 devices, the MoO_x layer was deposited through a shadow mask. For the module fabrication, after MoO_x deposition, the ZnO, BHJ and MoO_x layers were mechanically scribed into nine units based on the cathode pattern to separate devices and expose one edge of each cathode for series connection. Then 16 nm thick Ag was thermally

evaporated at 0.1 Å/s (100 nm Ag at 0.1-0.6 Å/s, for opaque devices) through a shadow mask followed by 100 nm Ag grid deposition at 0.1-0.6 Å/s through the Kapton shadow mask to construct the anode. The anode has a 1 cm² overlap with the cathode pattern to define the unit device area and to connect the unit cells in series along a column. The outcoupling structure was thermally evaporated in a high vacuum chamber (base pressure $\sim 10^{-7}$ Torr) at 0.5 Å/s for each layer.

The current density-voltage (J - V) characteristics and external quantum efficiency (EQE) of 4 mm² and 1 cm² devices were measured in a glovebox filled with ultrapure nitrogen ($O_2 < 0.1$ ppm, $H_2O < 0.1$ ppm). The specific series resistance is fitted then from the linear region of dark J - V curve. Light from a Xe lamp was filtered to achieve a simulated AM 1.5G spectrum (American Society for Testing and Materials, ASTM G173-03) whose 1 sun intensity was calibrated by a National Renewable Energy Laboratory certified Si reference cell to measure illuminated J - V characteristics. The EQE measurements were performed with a 200 Hz-chopped, monochromated and focused beam from a Xe lamp, the beam is focused to underfill the device area, for the devices with grids the beam can underfill the device area between grids. The current-voltage characteristics of 9 cm² active area module were measured in air using a solar simulator with a 1000 W Xe lamp with an AM 1.5G filter (Oriel Instruments, Model 91191) whose 1 sun intensity was calibrated by a Si reference cell. The transmission spectra were measured using UV-vis spectrometer (Perkin-Elmer 1050). The reflection spectra were measured using an F20 Filmetric thin film measurement instrument integrated with a spectrometer and a light source from 395 nm to 1032 nm.

The average photopic transmission (APT) is calculated using the formula:^{14,15,43}

$$APT = \frac{\int T(\lambda)P(\lambda)S(\lambda)d\lambda}{\int P(\lambda)S(\lambda)d\lambda}$$

where λ is wavelength, T is the transmission, P is the photopic spectral response of human eyes, and S is the AM 1.5G solar irradiance, which is the incident light spectrum of a solar cell. APT has also been referred to as average visible transmission (AVT).^{5,17,18,44–48} However, AVT is also understood as the average transmittance in the visible region.^{18,27,49,50} Hence, APT as defined above eliminates that ambiguity.

Acknowledgement

This work is supported by the U.S. Department of Energy’s Office of Energy Efficiency and Renewable Energy (EERE) under Solar Energy Technologies Office (SETO) Agreement Number DE-EE0008561. The authors would also like to acknowledge Universal Display Corporation for funding of this work.

Table I. 4 mm², 1 cm² PCE-10:BT-CIC OPV and 9 cm² mini-module performance under simulated AM 1.5G illumination at 1 sun intensity

Device	J_{SC} (mA/cm ²)	V_{OC} (V)	FF	PCE (%)	R_{SA} ($\Omega \cdot \text{cm}^2$)	APT (%)
Opaque						
4 mm ²	23.5 ± 0.8	0.69 ± 0.01	0.69 ± 0.01	11.2 ± 0.4	1.5 ± 0.1	-
1 cm ²	23.1 ± 0.7	0.69 ± 0.01	0.39 ± 0.03	5.9 ± 0.3	15.4 ± 0.5	-
1 cm ² w/ bottom grid	22.0 ± 0.4	0.69 ± 0.01	0.65 ± 0.01	10.0 ± 0.2	3.1 ± 0.4	-
Semitransparent (ST)						
4 mm ²	17.5 ± 0.6	0.68 ± 0.01	0.69 ± 0.01	8.2 ± 0.3	1.8 ± 0.1	-
1 cm ² w/ bottom grid	16.2 ± 0.3	0.68 ± 0.01	0.57 ± 0.01	6.3 ± 0.2	9.5 ± 0.3	-

1 cm ² w/ bottom and top grids	16.5 ± 0.1	0.68 ± 0.01	0.65 ± 0.01	7.3 ± 0.1	4.3 ± 0.2	20.0 ± 1.0
1 cm ² w/ both grids and OC	16.3 ± 0.2	0.68 ± 0.01	0.66 ± 0.01	7.3 ± 0.1	-	38.1 ± 1.1
ST Module						
1 cm ² discrete cell	16.8 ± 0.3	0.67 ± 0.01	0.63 ± 0.01	7.2 ± 0.2	-	38.1 ± 1.1
module	5.7 ± 0.1 (<i>I</i> _{SC} = 51.1 ± 1.0 mA)	2.00 ± 0.01	0.63 ± 0.01	7.2 ± 0.1	-	38.1 ± 1.1

References

- (1) Pagliaro, M.; Ciriminna, R.; Palmisano, G. BIPV: Merging the Photovoltaic with the Construction Industry. *Prog. Photovoltaics Res. Appl.* **2010**, *18* (1), 61–72.
<https://doi.org/10.1002/pip.920>.
- (2) Yang, R. J.; Zou, P. X. W. Building Integrated Photovoltaics (BIPV): Costs, Benefits, Risks, Barriers and Improvement Strategy. *Int. J. Constr. Manag.* **2016**, *16* (1), 39–53.
<https://doi.org/10.1080/15623599.2015.1117709>.
- (3) Ferrara, C.; Wilson, H. R.; Sprenger, W. Building-Integrated Photovoltaics (BIPV). In *The Performance of Photovoltaic (PV) Systems: Modelling, Measurement and Assessment*; Elsevier Inc., 2017; pp 235–250. <https://doi.org/10.1016/B978-1-78242-336-2.00008-2>.
- (4) Heinsteins, P.; Ballif, C.; Perret-Aebi, L. E. Building Integrated Photovoltaics (BIPV): Review, Potentials, Barriers and Myths. *Green* **2013**, *3* (2), 125–156.
<https://doi.org/10.1515/green-2013-0020>.
- (5) Traverse, C. J.; Pandey, R.; Barr, M. C.; Lunt, R. R. Emergence of Highly Transparent Photovoltaics for Distributed Applications. *Nat. Energy* **2017**, *2* (11), 849–860.
<https://doi.org/10.1038/s41560-017-0016-9>.
- (6) Lunt, R. R.; Bulovic, V. Transparent, near-Infrared Organic Photovoltaic Solar Cells for Window and Energy-Scavenging Applications. *Appl. Phys. Lett.* **2011**, *98* (11), 113305. <https://doi.org/10.1063/1.3567516>.
- (7) Meiss, J.; Holzmueller, F.; Gresser, R.; Leo, K.; Riede, M. Near-Infrared Absorbing Semitransparent Organic Solar Cells. *Appl. Phys. Lett.* **2011**, *99* (19), 10–13.

- <https://doi.org/10.1063/1.3660708>.
- (8) Li, Y.; Lin, J. D.; Che, X.; Qu, Y.; Liu, F.; Liao, L. S.; Forrest, S. R. High Efficiency Near-Infrared and Semitransparent Non-Fullerene Acceptor Organic Photovoltaic Cells. *J. Am. Chem. Soc.* **2017**, *139* (47), 17114–17119.
<https://doi.org/10.1021/jacs.7b11278>.
 - (9) Che, X.; Li, Y.; Qu, Y.; Forrest, S. R. High Fabrication Yield Organic Tandem Photovoltaics Combining Vacuum- and Solution-Processed Subcells with 15% Efficiency. *Nat. Energy* **2018**, *3* (5), 422–427. <https://doi.org/10.1038/s41560-018-0134-z>.
 - (10) Meng, L.; Zhang, Y.; Wan, X.; Li, C.; Zhang, X.; Wang, Y.; Ke, X.; Xiao, Z.; Ding, L.; Xia, R.; et al. Organic and Solution-Processed Tandem Solar Cells with 17.3% Efficiency. *Science* **2018**, *361* (6407), 1094–1098.
<https://doi.org/10.1126/science.aat2612>.
 - (11) Liu, Q.; Jiang, Y.; Jin, K.; Qin, J.; Xu, J.; Li, W.; Xiong, J.; Liu, J.; Xiao, Z.; Sun, K.; et al. 18% Efficiency Organic Solar Cells. *Sci. Bull.* **2020**, *65* (4), 272–275.
<https://doi.org/10.1016/j.scib.2020.01.001>.
 - (12) Cui, Y.; Yao, H.; Zhang, J.; Xian, K.; Zhang, T.; Hong, L.; Wang, Y.; Xu, Y.; Ma, K.; An, C.; et al. Single-Junction Organic Photovoltaic Cells with Approaching 18% Efficiency. *Adv. Mater.* **2020**, *32* (19). <https://doi.org/10.1002/adma.201908205>.
 - (13) Burlingame, Q.; Huang, X.; Liu, X.; Jeong, C.; Coburn, C.; Forrest, S. R. Intrinsically Stable Organic Solar Cells under High-Intensity Illumination. *Nature* **2019**, *573* (7774), 394–397. <https://doi.org/10.1038/s41586-019-1544-1>.

- (14) Li, Y.; Ji, C.; Qu, Y.; Huang, X.; Hou, S.; Li, C. Z.; Liao, L. S.; Guo, L. J.; Forrest, S. R. Enhanced Light Utilization in Semitransparent Organic Photovoltaics Using an Optical Outcoupling Architecture. *Adv. Mater.* **2019**, *31* (40), 1903173.
<https://doi.org/10.1002/adma.201903173>.
- (15) Li, Y.; Guo, X.; Peng, Z.; Qu, B.; Yan, H.; Ade, H.; Zhang, M.; Forrest, S. R. Color-Neutral, Semitransparent Organic Photovoltaics for Power Window Applications. *Proc. Natl. Acad. Sci. U. S. A.* **2020**, *117* (35), 21147–21154.
<https://doi.org/10.1073/pnas.2007799117>.
- (16) Bai, Y.; Zhao, C.; Chen, X.; Zhang, S.; Zhang, S.; Hayat, T.; Alsaedi, A.; Tan, Z.; Hou, J.; Li, Y. Interfacial Engineering and Optical Coupling for Multicolored Semitransparent Inverted Organic Photovoltaics with a Record Efficiency of over 12%. *J. Mater. Chem. A* **2019**, *7* (26), 15887–15894.
<https://doi.org/10.1039/c9ta05789g>.
- (17) Liu, Q.; Gerling, L. G.; Bernal-Texca, F.; Toudert, J.; Li, T.; Zhan, X.; Martorell, J. Light Harvesting at Oblique Incidence Decoupled from Transmission in Organic Solar Cells Exhibiting 9.8% Efficiency and 50% Visible Light Transparency. *Adv. Energy Mater.* **2020**, *10* (17), 1904196. <https://doi.org/10.1002/aenm.201904196>.
- (18) Zuo, L.; Shi, X.; Fu, W.; Jen, A. K. Y. Highly Efficient Semitransparent Solar Cells with Selective Absorption and Tandem Architecture. *Adv. Mater.* **2019**, *31* (36), 1901683. <https://doi.org/10.1002/adma.201901683>.
- (19) Dai, S.; Zhan, X. Nonfullerene Acceptors for Semitransparent Organic Solar Cells. *Adv. Energy Mater.* **2018**, *8* (21), 1800002. <https://doi.org/10.1002/aenm.201800002>.

- (20) Brus, V. V.; Lee, J.; Luginbuhl, B. R.; Ko, S. J.; Bazan, G. C.; Nguyen, T. Q. Solution-Processed Semitransparent Organic Photovoltaics: From Molecular Design to Device Performance. *Adv. Mater.* **2019**, *31* (30), 1900904.
<https://doi.org/10.1002/adma.201900904>.
- (21) Chen, S.; Yao, H.; Hu, B.; Zhang, G.; Arunagiri, L.; Ma, L. K.; Huang, J.; Zhang, J.; Zhu, Z.; Bai, F.; et al. A Nonfullerene Semitransparent Tandem Organic Solar Cell with 10.5% Power Conversion Efficiency. *Adv. Energy Mater.* **2018**, *8* (31), 1–6.
<https://doi.org/10.1002/aenm.201800529>.
- (22) Wang, D.; Qin, R.; Zhou, G.; Li, X.; Xia, R.; Li, Y.; Zhan, L.; Zhu, H.; Lu, X.; Yip, H. L.; et al. High-Performance Semitransparent Organic Solar Cells with Excellent Infrared Reflection and See-Through Functions. *Adv. Mater.* **2020**, *32* (32), 2001621.
<https://doi.org/10.1002/adma.202001621>.
- (23) Lee, B.; Lahann, L.; Li, Y.; Forrest, S. R. Cost Estimates of Production Scale Semitransparent Organic Photovoltaic Modules for Building Integrated Photovoltaics. *Sustain. Energy Fuels* **2020**, *4* (11), 5765–5772. <https://doi.org/10.1039/d0se00910e>.
- (24) Xiao, X.; Lee, K.; Forrest, S. R. Scalability of Multi-Junction Organic Solar Cells for Large Area Organic Solar Modules. *Appl. Phys. Lett.* **2015**, *106* (21).
<https://doi.org/10.1063/1.4921771>.
- (25) Dong, S.; Jia, T.; Zhang, K.; Jing, J.; Huang, F. Single-Component Non-Halogen Solvent-Processed High-Performance Organic Solar Cell Module with Efficiency over 14%. *Joule* **2020**, *4* (9), 2004–2016. <https://doi.org/10.1016/j.joule.2020.07.028>.
- (26) Lim, D. C.; Jeong, J. H.; Hong, K.; Nho, S.; Lee, J.-Y.; Hoang, Q. V.; Lee, S. K.; Pyo,

- K.; Lee, D.; Cho, S. Semi-Transparent Plastic Solar Cell Based on Oxide-Metal-Oxide Multilayer Electrodes. *Prog. Photovoltaics Res. Appl.* **2018**, *26* (3), 188–195.
<https://doi.org/10.1002/pip.2965>.
- (27) Pascual-San-José, E.; Sadoughi, G.; Lucera, L.; Stella, M.; Martínez-Ferrero, E.; Morse, G. E.; Campoy-Quiles, M.; Burgués-Ceballos, I. Towards Photovoltaic Windows: Scalable Fabrication of Semitransparent Modules Based on Non-Fullerene Acceptors via Laser-Patterning. *J. Mater. Chem. A* **2020**, *8* (19), 9882–9895.
<https://doi.org/10.1039/d0ta02994g>.
- (28) Berny, S.; Blouin, N.; Distler, A.; Egelhaaf, H.-J.; Krompiec, M.; Lohr, A.; Lozman, O. R.; Morse, G. E.; Nanson, L.; Pron, A.; et al. Solar Trees: First Large-Scale Demonstration of Fully Solution Coated, Semitransparent, Flexible Organic Photovoltaic Modules. *Adv. Sci.* **2016**, *3* (5), 1500342.
<https://doi.org/10.1002/advs.201500342>.
- (29) Guo, F.; Kubis, P.; Przybilla, T.; Spiecker, E.; Forberich, K.; Brabec, C. J. Semitransparent Organic Photovoltaic Modules with Ag Nanowire Top Electrodes. In *Organic Photovoltaics XV*; Kafafi, Z. H., Lane, P. A., Samuel, I. D. W., Eds.; SPIE, 2014; Vol. 9184, p 91841D. <https://doi.org/10.1117/12.2058288>.
- (30) Guo, F.; Kubis, P.; Przybilla, T.; Spiecker, E.; Hollmann, A.; Langner, S.; Forberich, K.; Brabec, C. J. Nanowire Interconnects for Printed Large-Area Semitransparent Organic Photovoltaic Modules. *Adv. Energy Mater.* **2015**, *5* (12), 1401779.
<https://doi.org/10.1002/aenm.201401779>.
- (31) Strohm, S.; Machui, F.; Langner, S.; Kubis, P.; Gasparini, N.; Salvador, M.;

- McCulloch, I.; Egelhaaf, H. J.; Brabec, C. J. P3HT: Non-Fullerene Acceptor Based Large Area, Semi-Transparent PV Modules with Power Conversion Efficiencies of 5%, Processed by Industrially Scalable Methods. *Energy Environ. Sci.* **2018**, *11* (8), 2225–2234. <https://doi.org/10.1039/c8ee01150h>.
- (32) Lucera, L.; Machui, F.; Schmidt, H. D.; Ahmad, T.; Kubis, P.; Strohm, S.; Hepp, J.; Vetter, A.; Egelhaaf, H. J.; Brabec, C. J. Printed Semi-Transparent Large Area Organic Photovoltaic Modules with Power Conversion Efficiencies of Close to 5 %. *Org. Electron.* **2017**, *45*, 209–214. <https://doi.org/10.1016/j.orgel.2017.03.013>.
- (33) Jeong, J. H.; Jahandar, M.; Prasetyo, A.; Kim, J. M.; Kim, J. H.; Kim, S.; Lim, D. C. Multi-Dimensional Interfacial Engineering for a Practical Large-Area Transparent Flexible Organic Photovoltaics. *Chem. Eng. J.* **2021**, *419*, 129672. <https://doi.org/10.1016/j.cej.2021.129672>.
- (34) Lewis, J. E.; Lafalce, E.; Togli, P.; Jiang, X. Over 30% Transparency Large Area Inverted Organic Solar Array by Spray. *Sol. Energy Mater. Sol. Cells* **2011**, *95* (10), 2816–2822. <https://doi.org/10.1016/j.solmat.2011.05.037>.
- (35) Bube, R. H.; Fahrenbruch, A. L. Photovoltaic Effect. *Adv. Electron. Electron Phys.* **1981**, *56* (C), 163–217. [https://doi.org/10.1016/S0065-2539\(08\)60424-2](https://doi.org/10.1016/S0065-2539(08)60424-2).
- (36) Hauser, J. R.; Dunbar, P. M. Performance Limitations of Silicon Solar Cells. *IEEE Trans. Electron Devices* **1977**, *ED-24* (4), 305–321. <https://doi.org/10.1109/T-ED.1977.18734>.
- (37) Wang, Y.; Wang, G.; Xing, Y.; Adil, M. A.; Memon, W. A.; Chang, Y.; Liu, L.; Yang, C.; Zhang, M.; Li, D.; et al. Top and Bottom Electrode Optimization Enabled High-

- Performance Flexible and Semi-Transparent Organic Solar Cells. *Mater. Chem. Front.* **2021**, 3 (1). <https://doi.org/10.1039/D1QM00151E>.
- (38) Rowell, M. W.; McGehee, M. D. Transparent Electrode Requirements for Thin Film Solar Cell Modules. *Energy Environ. Sci.* **2011**, 4 (1), 131–134. <https://doi.org/10.1039/c0ee00373e>.
- (39) Patil, B. R.; Mirsafaei, M.; Cielecki, P. P.; Cauduro, A. L. F.; Fiutowski, J.; Rubahn, H. G.; Madsen, M. ITO with Embedded Silver Grids as Transparent Conductive Electrodes for Large Area Organic Solar Cells. *Nanotechnology* **2017**, 28 (40), 405303. <https://doi.org/10.1088/1361-6528/aa820a>.
- (40) Davy, N. C.; Sezen-Edmonds, M.; Gao, J.; Lin, X.; Liu, A.; Yao, N.; Kahn, A.; Loo, Y.-L. Pairing of Near-Ultraviolet Solar Cells with Electrochromic Windows for Smart Management of the Solar Spectrum. *Nat. Energy* **2017**, 2 (8), 1–11. <https://doi.org/10.1038/nenergy.2017.104>.
- (41) Distler, A.; Brabec, C. J.; Egelhaaf, H. J. Organic Photovoltaic Modules with New World Record Efficiencies. *Prog. Photovoltaics Res. Appl.* **2021**, 29 (1), 24–31. <https://doi.org/10.1002/pip.3336>.
- (42) Sun, R.; Wu, Q.; Guo, J.; Wang, T.; Wu, Y.; Qiu, B.; Luo, Z.; Yang, W.; Hu, Z.; Guo, J.; et al. A Layer-by-Layer Architecture for Printable Organic Solar Cells Overcoming the Scaling Lag of Module Efficiency. *Joule* **2020**, 4 (2), 407–419. <https://doi.org/10.1016/j.joule.2019.12.004>.
- (43) Forrest, S. R. Organic Light Detectors. In *Organic Electronics*; 2020. <https://doi.org/10.1093/oso/9780198529729.003.0007>.

- (44) Almora, O.; Baran, D.; Bazan, G. C.; Berger, C.; Cabrera, C. I.; Catchpole, K. R.; Erten-Ela, S.; Guo, F.; Hauch, J.; Ho-Baillie, A. W. Y.; et al. Device Performance of Emerging Photovoltaic Materials (Version 1). *Adv. Energy Mater.* **2021**, *11* (11), 2002774. <https://doi.org/10.1002/aenm.202002774>.
- (45) Li, Z.; Ma, T.; Yang, H.; Lu, L.; Wang, R. Transparent and Colored Solar Photovoltaics for Building Integration. *Sol. RRL* **2021**, *5* (3), 2000614. <https://doi.org/10.1002/solr.202000614>.
- (46) Lee, K.; Kim, N.; Kim, K.; Um, H. D.; Jin, W.; Choi, D.; Park, J.; Park, K. J.; Lee, S.; Seo, K. Neutral-Colored Transparent Crystalline Silicon Photovoltaics. *Joule* **2020**, *4* (1), 235–246. <https://doi.org/10.1016/j.joule.2019.11.008>.
- (47) Yang, C.; Liu, D.; Bates, M.; Barr, M. C.; Lunt, R. R. How to Accurately Report Transparent Solar Cells. *Joule* **2019**, *3* (8), 1803–1809. <https://doi.org/10.1016/j.joule.2019.06.005>.
- (48) Lee, K.; Um, H. D.; Choi, D.; Park, J.; Kim, N.; Kim, H.; Seo, K. The Development of Transparent Photovoltaics. *Cell Reports Phys. Sci.* **2020**, *1* (8), 100143. <https://doi.org/10.1016/j.xcrp.2020.100143>.
- (49) Chen, K. S.; Salinas, J. F.; Yip, H. L.; Huo, L.; Hou, J.; Jen, A. K. Y. Semi-Transparent Polymer Solar Cells with 6% PCE, 25% Average Visible Transmittance and a Color Rendering Index Close to 100 for Power Generating Window Applications. *Energy Environ. Sci.* **2012**, *5* (11), 9551–9557. <https://doi.org/10.1039/c2ee22623e>.
- (50) Godfroy, M.; Liotier, J.; Mwalukuku, V. M.; Joly, D.; Hualmé, Q.; Cabau, L.;

Aumaitre, C.; Kervella, Y.; Narbey, S.; Oswald, F.; et al. Benzothiadiazole-Based Photosensitizers for Efficient and Stable Dye-Sensitized Solar Cells and 8.7% Efficiency Semi-Transparent Mini-Modules. *Sustain. Energy Fuels* **2021**, 5 (1), 144–153. <https://doi.org/10.1039/d0se01345e>.

Figure Captions

Figure 1. Schematic of the 1 cm² semitransparent organic photovoltaic (ST-OPV) device structure composed of electrodes with integrated grids, heterojunction and optical outcoupling (OC) layers.

Figure 2. (a) Current density-voltage (J - V) characteristics of 4 mm² (red, square), 1 cm² (blue, circle), and 1 cm² cathode with grids (yellow, triangle) OPV devices. (b) J - V characteristics of 4 mm² (red, square), 1 cm² (blue, circle) and 1 cm² anode with grids (yellow, triangle) ST-OPV devices. (c) J - V characteristics and (d) external quantum efficiency (EQE) spectra of 1 cm² ST-OPV cells with (blue, circle) and without (red, square) the OC structure. (e) Transmission and reflection spectra of the ST-OPV stack with (blue, circle) and without (red, square) the OC structure.

Figure 3. Schematic of the series-parallel connected module design.

Figure 4. (a) Power conversion efficiencies of the separate unit cells across the module. (b) Current-voltage (I - V) characteristics of a discrete cell (black, circle) and the module (red, square) under simulated 1 sun illumination. Inset: Photograph of the ST-OPV module.

Figure 5. Fabrication flow of Kapton shadow mask for top electrode grids patterning.

Fig. 1

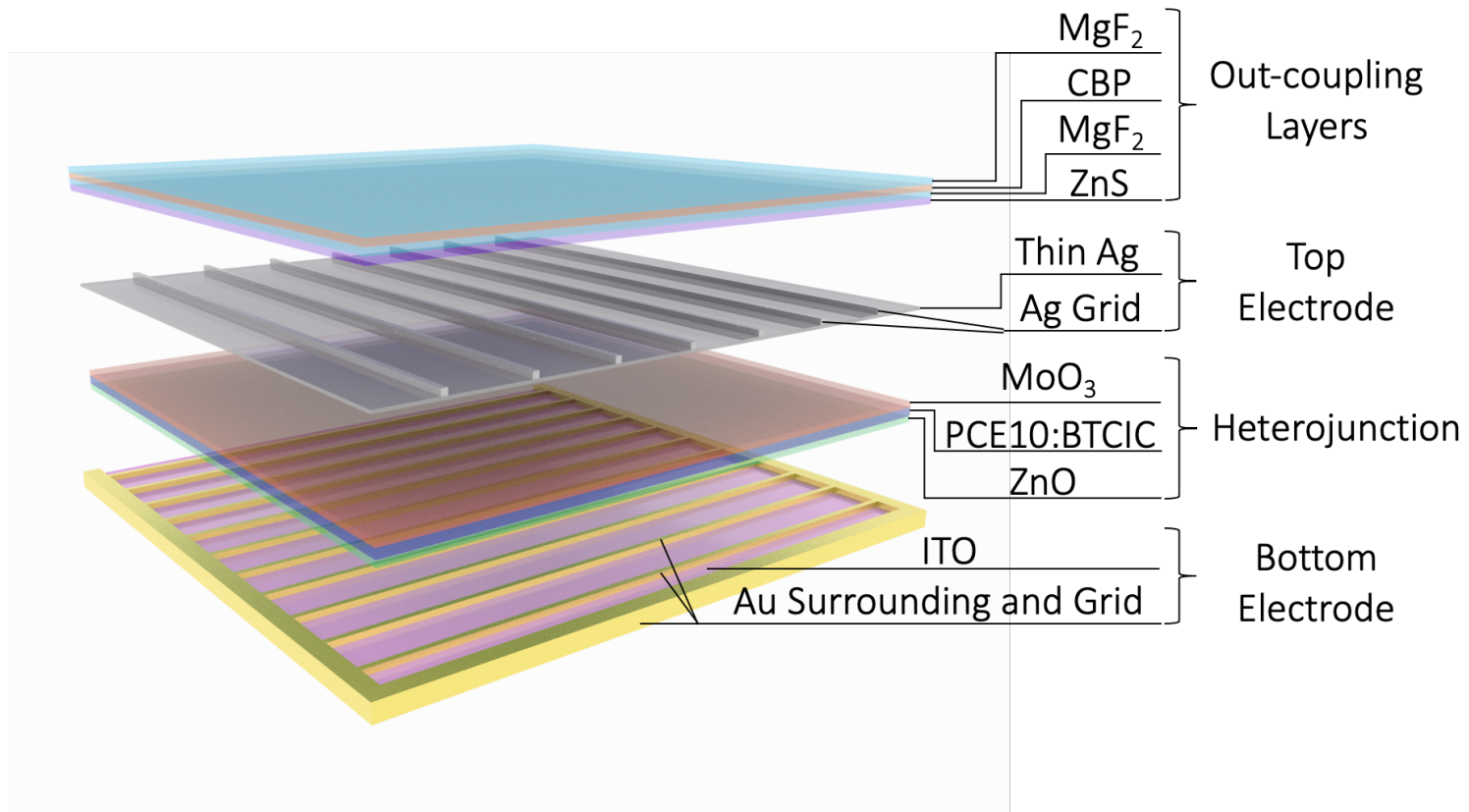


Fig. 2

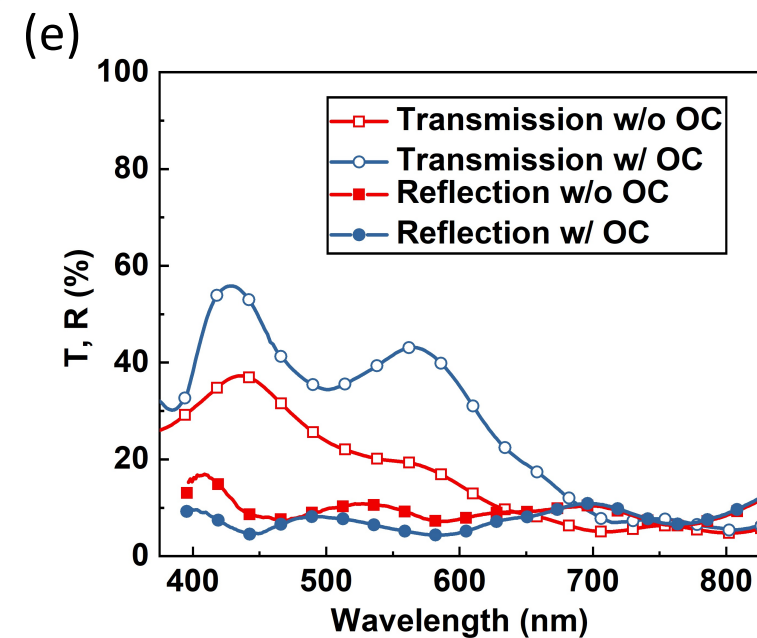
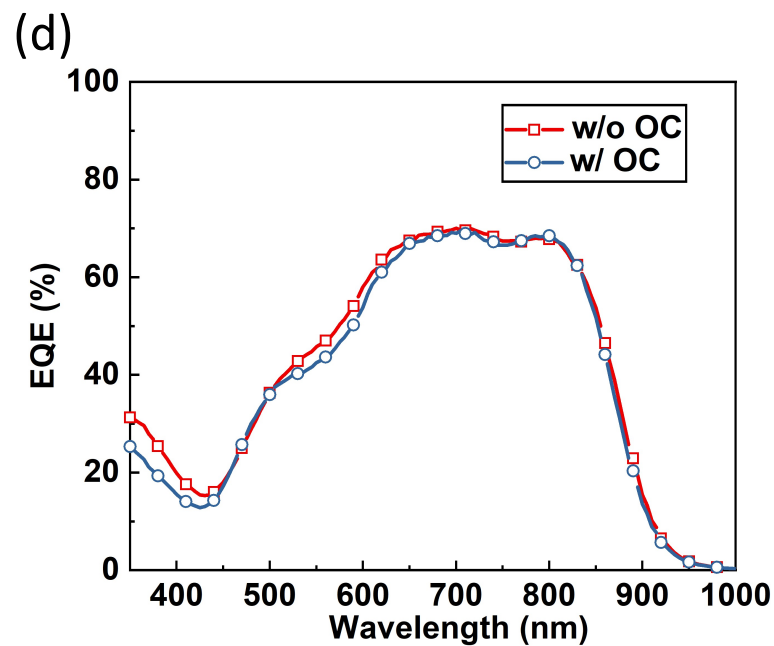
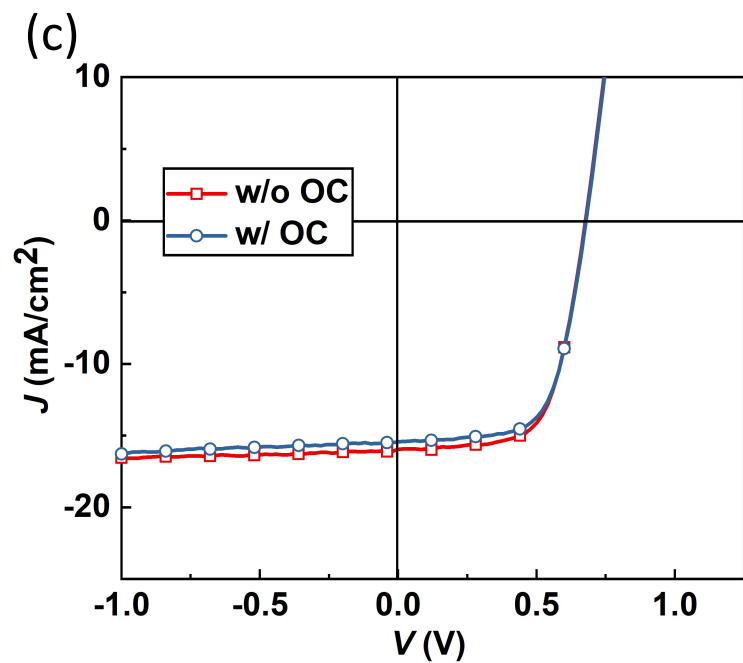
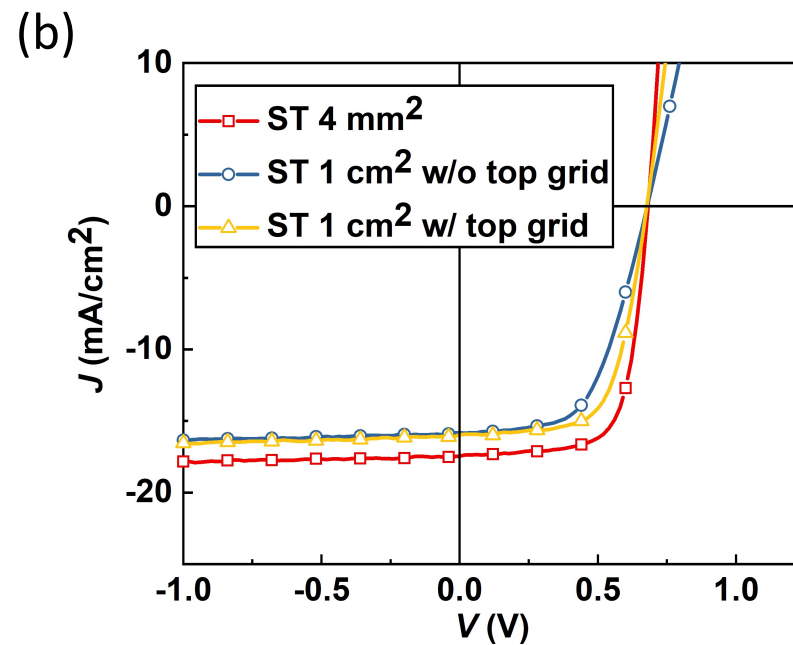
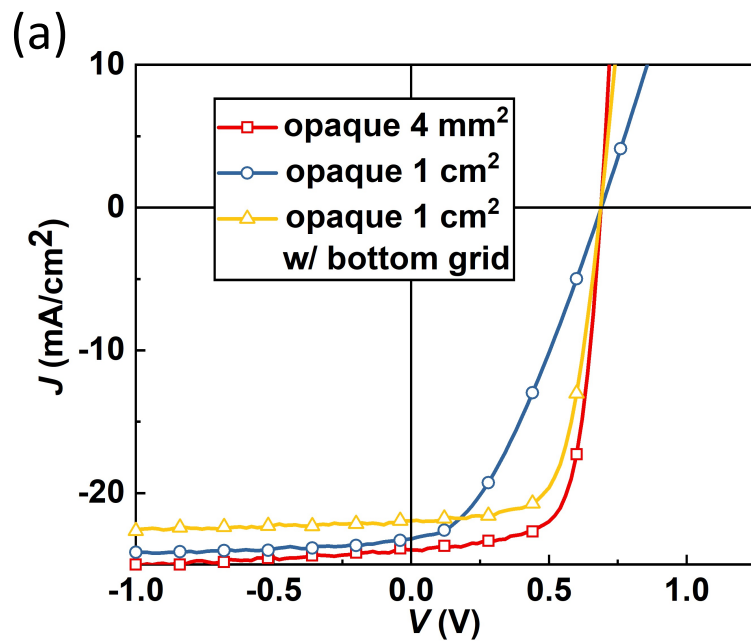
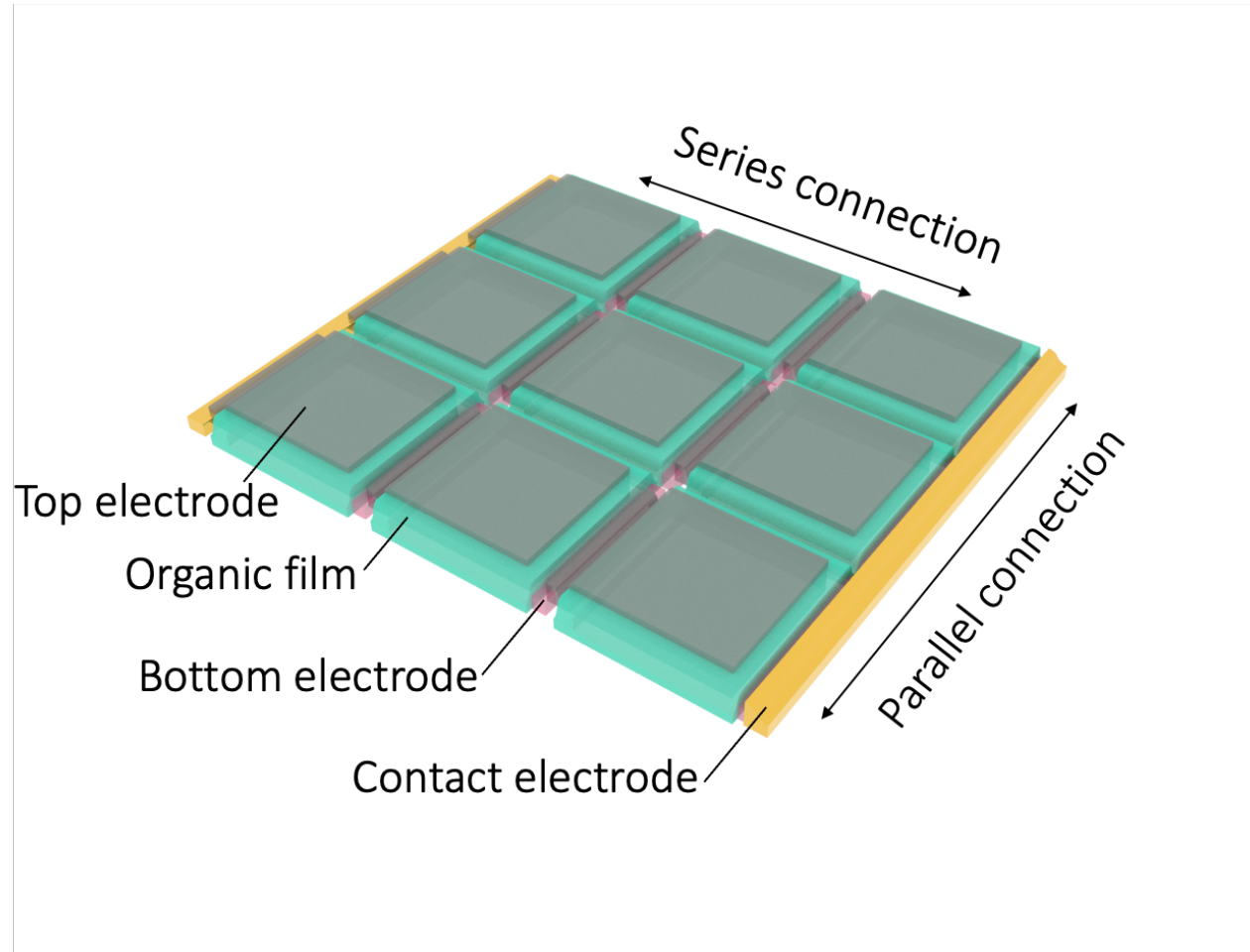
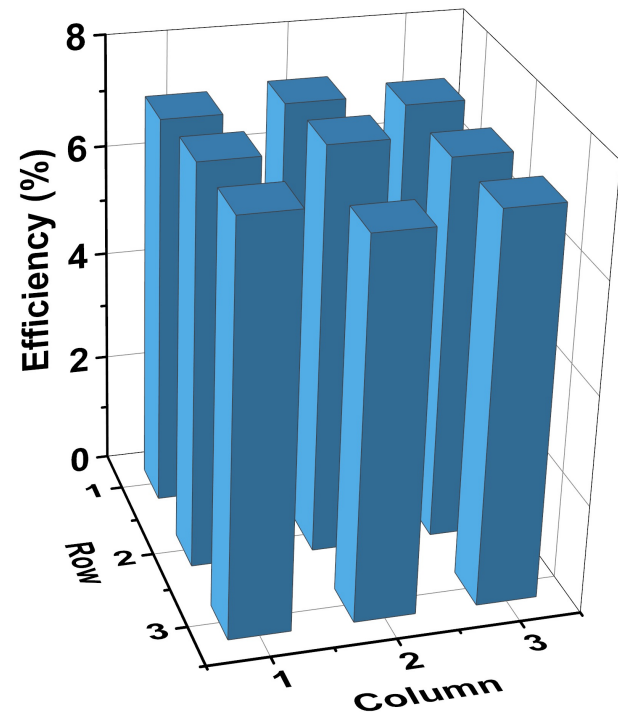


Fig. 3



(a)



(b)

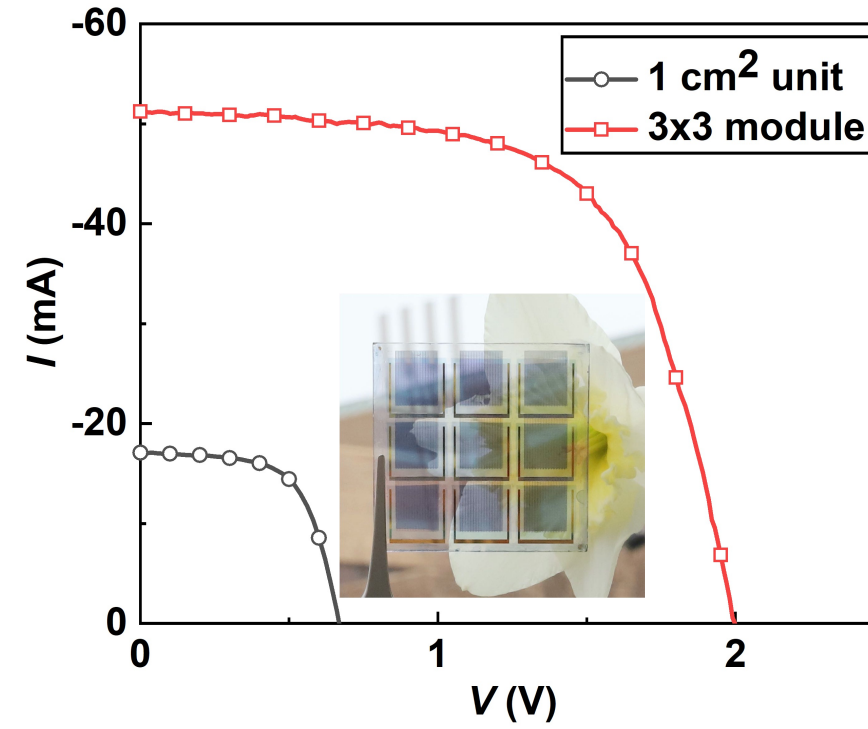


Fig. 5

